ACS OMEGA

Open Access



http://pubs.acs.org/journal/acsodf

Article

# Impact of Co-Doping on the Visible Light-Driven Photocatalytic and Photoelectrochemical Activities of $Eu(OH)_3$

Shaidatul Najihah Matussin, Fazlurrahman Khan, Mohammad Hilni Harunsani, Young-Mog Kim, and Mohammad Mansoob Khan*

Cite This: *ACS Omega* 2024, 9, 16420−16428

Read Online

ACCESS | Metrics & More | Article Recommendations | Supporting Information

**ABSTRACT:** The microwave-assisted synthesis approach was used to synthesize $Eu(OH)_3$ and $Co-Eu(OH)_3$ nanorods. Various techniques were used to investigate the structural, optical, and morphological features of the $Eu(OH)_3$ and $Co-Eu(OH)_3$ NRs. Both $Eu(OH)_3$ and $Co-Eu(OH)_3$ NRs were found to be hexagonal with crystallite sizes ranging from 21 to 35 nm. FT-IR and Raman spectra confirmed the formation of $Eu(OH)_3$ and $Co-Eu(OH)_3$. Rod-shaped $Eu(OH)_3$ and $Co-Eu(OH)_3$ with average lengths and diameters ranging from 27 to 50 nm and 8 to 12 nm, respectively, were confirmed by TEM. The addition of Co was found to increase the particle size. Furthermore, with increased Co doping, the band gap energies of $Co-Eu(OH)_3$ NRs were lowered (3.80−2.49 eV) in comparison to $Eu(OH)_3$, and the PL intensities with Co doping were quenched, suggesting the lessening of electron/hole recombination. The effect of these altered properties of $Eu(OH)_3$ and $Co-Eu(OH)_3$ was observed through the photocatalytic degradation of brilliant green dye (BG) and photoelectrochemical activity. In the photocatalytic degradation of BG, 5% $Co-Eu(OH)_3$ had the highest response. However, photoelectrochemical experiments suggested that 10% $Co-Eu(OH)_3$ NRs showed improved activity when exposed to visible light. As a result, $Co-Eu(OH)_3$ NRs have the potential to be a promising visible-light active material for photocatalysis.

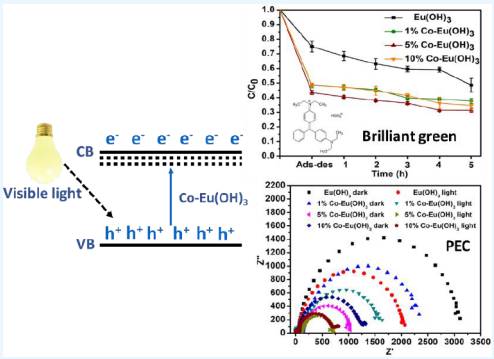


## 1. INTRODUCTION

Rare-earth metal oxides (REMO) have piqued the interest of researchers for many years due to their remarkable optical, magnetic, electric, and catalytic capabilities resulting from their unique 4*f* electron configuration.[1−4] REMO can be easily produced by dehydrating their respective hydroxides.[5] These materials are in great demand, and their chemical, catalytic, electromagnetic, magnetic, and optical features are vital in a wide range of applications.[6−8] The properties of REMO are greatly influenced by their morphologies and sizes. Various morphologies of REMO have been explored, such as spherical,[9,10] rod-like,[11] spindle-like,[12] flower-like,[13], and sheet-like.[14] With the aim of achieving the specific properties for further applications, the selection of well-defined synthetic methods is required.[15]

Among REMO, europium(III) oxides ($Eu_2O_3$) is regarded as one of the finest phosphors and has received attention as a candidate for high-k gate-dielectric material owing to its dielectric constant of 14 and a band gap energy of 4.4 eV.[16] Moreover, owing to red emission characteristic of $5D_0 - 7F_J$ ($J$ = 0, 1, 2, 3, 4) transition of Eu(III), it has become an important rare-earth oxide.[17] $Eu^{3+}$ luminescence is particularly interesting as its major emission band is centered near 612 nm (red). Therefore, $Eu^{3+}$ is a good activator with a sharp and intense luminescence in the red region of the visible spectrum. $Eu_2O_3$ has been widely investigated for their potential applications ranging from color display to biomedical sensors.[18,19]

Furthermore, europium(III) hydroxide ($Eu(OH)_3$) is very significant as it has good electrical, optical, catalytic, and chemical characteristics resulting from electron transitions inside the 4*f* shell.[20−22] Many investigations have been conducted to synthesize $Eu(OH)_3$. For example, Wei et al. reported that $Eu(OH)_3$ was synthesized using a hydrothermal method at 150 °C for 60 min.[23] The acquired $Eu(OH)_3$ was rod-like with an estimated length of 80−160 nm and a diameter of 25−40 nm. Kang et al. have also employed a hydrothermal method to produce $Eu(OH)_3$ at 120 °C for 12 h.[18] $Eu(OH)_3$ had rod-like morphology with diameters of 50−150 nm and lengths of 500 nm −2 $\mu$m. Zhang et al. synthesized $Eu(OH)_3$ using a typical precipitation process.[24] In this case, $Eu(OH)_3$ nanospindles with 200−600 nm in length and 80−160 nm in diameter were obtained. Furthermore, $Eu(OH)_3$ has been employed in a variety of applications, such as photocatalysis,[21]

**Received:** January 3, 2024
**Revised:** January 13, 2024
**Accepted:** January 18, 2024
**Published:** March 28, 2024

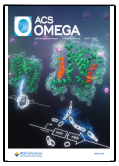

antibacterial studies,[25] bioimaging,[26] and sensors.[27] In addition, dopants with different ionic states have been introduced into the $Eu(OH)_3$ lattice, which may cause more structural modification and defects to achieve charge neutrality, enhancing physical properties and biocompatibility.[28]

Nonbiodegradable organic dyes have been found and widely spread in industrial wastewater originating from the paper, textile, and garment industries.[29,30] Even in low quantities, these dye-polluted effluents are toxic to living organisms.[31] Hence, removing dyes from wastewater is important. Aside from that, redox reactions have shown promising water treatment activity as the reaction products may be easily isolated and removed.[32] Owing to this, researchers have adapted electrochemical systems to a variety of functional applications, including photovoltaics,[33] fuel cells,[34] supercapacitors,[35] as well as sensors.[36]

Therefore, in this work, $Eu(OH)_3$ and Co-doped $Eu(OH)_3$ ($Co-Eu(OH)_3$) were synthesized by using a microwave-assisted synthesis method. To the best of the authors' knowledge, there is no report on the microwave-assisted synthesis of $Co-Eu(OH)_3$. Several approaches were used to investigate the structural, optical, and morphological features of the $Eu(OH)_3$ and $Co-Eu(OH)_3$ NRs. The photocatalytic degradation of brilliant green (BG) was studied for 5 h utilizing $Eu(OH)_3$ and 1%, 5%, and 10% $Co-Eu(OH)_3$. The photoelectrochemical studies, namely, linear sweep voltammetry (LSV) and electrochemical impedance spectroscopy (EIS) were also carried out in the dark and under visible light conditions using $Na_2O_3$ as the electrolyte.

## 2. EXPERIMENTAL SECTION

**2.1. Instruments Used.** The synthesis of $Eu(OH)_3$ and $Co-Eu(OH)_3$ was carried out using a microwave reactor (Anton Paar Monowave 400, Austria). X-ray diffraction (XRD) analysis of the synthesized materials was carried out using a Shimadzu XRD-7000 X-ray diffractometer with Cu K$\alpha$ radiation ($\lambda$ = 1.5418) and a step size of 0.026°. Vibrational bands related to the formation of $Eu(OH)_3$ and $Co-Eu(OH)_3$ NRs were identified using Fourier-transform tnfrared spectroscopy (FT-IR, Shimadzu IRPrestige-21 Fourier Transform-Infrared Spectrophotometer) in the range of 450−4000 $cm^{-1}$. A Raman spectrometer (NRS-5100, JASCO) was utilized to study $Eu(OH)_3$ and Co- $Eu(OH)_3$ NRs at a laser wavelength of 785 nm with the maximum resolution of 1 $cm^{-1}$ in the range of 50−4000 $cm^{-1}$. Field-emission transmission electron microscopy (FE-TEM, JEM-F200 JEOL Ltd., Tokyo, Japan) was used for the investigation of the materials morphology with ultrathin carbon film supported copper grid at 200 kV and selected area electron diffraction (SAED). The band gap energy of the materials was investigated using UV−vis diffuse reflectance spectroscopy (DRS) (Shimadzu, UV-2600). X-ray photoelectron spectroscopy (XPS) was performed on Kratos Analytical, AXIS Nova with 225 W X-ray power from 286.69 to 1486.69 eV scan range for 1 cm × 1 cm analysis area. F-7000 Fluorescence spectroscopy (Hitachi High Tech) was utilized for the photoluminescence (PL) study of the materials with an excitation wavelength of 370 nm in the wavelength range of 200−900 nm. In order to study the photocatalytic activities of BG dye degradation, a Toption (TOPT-V) photochemical reactor irradiated by a 300 W xenon lamp was used and the absorbance of BG was observed using the UV−visible spectrophotometer (Shimadzu UV-1900, Japan). Autolab (Metrohm, United States) was utilized for the photoelectrochemical studies of $Eu(OH)_3$ and 1%, 5%, and 10% $Co-Eu(OH)_3$ NRs and visible light (Simon FL30 LED Floodlight, 100 W, China) was utilized in the experiment. The measurements were carried out using NOVA software.

**2.2. Chemicals Used.** For the synthesis, europium acetate hydrate ($Eu(CH_3COO)_3{\cdot}H_2O$, 99.9%) and cobalt dichloride hexahydrate ($CoCl_2{\cdot}6H_2O$) were obtained from Alfa-Aesar and Sigma-Aldrich, respectively. Water was purified using an aquatron (England) prior to use. For the photocatalytic reaction, brilliant green ($C_{27}H_{34}N_2O_4S$, 90%) was obtained from Sigma-Aldrich. Alpha-terpineol ($\alpha$-terpineol) and ethanol (95%) were obtained from Merck, and Daejung Chemicals and Metals Co. Ltd., respectively. Sodium sulfite ($Na_2SO_3$, 98%), ethyl cellulose 48−49.5% (w/w), and ethoxy basis were obtained from Sigma-Aldrich.

**2.3. Microwave-Assisted Synthesis of $Eu(OH)_3$ NRs.** $Eu(OH)_3$ NRs were synthesized using the microwave-assisted method as stated in the literature.[9,10] The $Eu(CH_3COO)_3{\cdot}H_2O$ solution (0.05 M, 15 mL) was prepared in a 30 mL microwave vessel, where 2.4 mL of 1 M NaOH was added slowly into the solution, forming a white precipitate. Next, the vessel was put inside a microwave reactor, and the temperature was slowly increased to 180 °C in 10 min and then maintained at 180 °C for 15 min, with the microwave power of 850 W. The product was then washed by centrifugation with distilled water for three times and dried at 80 °C. The percentage yield of the product was about 97% and it was coded as $Eu(OH)_3$.

**2.4. Microwave-Assisted Synthesis of $Co-Eu(OH)_3$ NRs.** The preparation of $Co-Eu(OH)_3$ NRs was conducted via the same microwave-assisted method as mentioned above. A $Eu(CH_3COO)_3{\cdot}H_2O$ (0.05 M, 15 mL) solution was prepared with a respective amount of $CoCl_2$ to synthesize 1%, 5%, and 10% $Co-Eu(OH)_3$ NRs. NaOH (2.4 mL, 1 M) was then added slowly to the solution. The synthesis reaction temperature was slowly heated to 180 °C in 10 min and then maintained at 180 °C for 15 min with the microwave power of 850 W. The product was washed by centrifugation with distilled water and it was dried at 80 °C. The percentage yield of the products was 95−97% and the products were coded as 1% $Co-Eu(OH)_3$, 5% $Co-Eu(OH)_3$, and 10% $Co-Eu(OH)_3$.

**2.5. Electrode Preparation.** The electrodes for photoelectrochemical study were prepared using the doctor blade method in which 25 mg of the respective samples was mixed with 0.5 mL ethanol and 0.5 mL $\alpha$-terpineol.[10] The mixture was sonicated for 10 min before 25 mg of ethyl cellulose was added to the mixture. The mixture was stirred at 80 °C for ∼2 h to produce a thick paste. The paste was then spread on fluorine-doped tin oxide (FTO) glass electrode of 2 cm × 1 cm in size using a doctor blade. The FTO glass electrodes were dried under a bulb for almost 3 h before they were put in an oven at 80 °C for 24 h for further drying.

**2.6. Photocatalytic Degradation of BG Dye.** $Eu(OH)_3$ and 1%, 5%, and 10% $Co-Eu(OH)_3$ were used for the photocatalytic degradation of the BG dye under visible light irradiation. In brief, 20 mg of $Eu(OH)_3$ and 1%, 5%, and 10% $Co-Eu(OH)_3$ NRs were put into 50 mL of 10 ppm of BG dye solution. The photocatalysis experiment was carried out following the literature.[9,10] The BG dye solution with the respective sample was sonicated for 3 min and proceeded with stirring in the dark for another 3 min. Then, the photocatalytic reaction was carried out with visible light irradiation (300 W) for 5 h. The absorbance of the BG solution at 620 nm was measured every 1 h using a UV−vis spectrophotometer. The percentage of


https://doi.org/10.1021/acsomega.3c10416
ACS Omega 2024, 9, 16420−16428

photocatalytic BG dye degradation was obtained using the following equation (eq 1):

$$\%\text{photocatalytic BG dye degradation} = \frac{(A_{\text{blank}} - A_{\text{sample}})}{A_{\text{blank}}} \times 100 \quad (1)$$

where $A_{\text{blank}}$ is the absorbance of BG only and $A_{\text{sample}}$ is the absorbance of BG after photocatalytic degradation reaction with the respective catalyst.

**2.7. Photoelectrochemical Studies.** Linear sweep voltammetry (LSV) and electrochemical impedance spectroscopy (EIS) of $Eu(OH)_3$ and $Co-Eu(OH)_3$ NRs were carried out to investigate their photoelectrochemical responses under visible light irradiation. The experiments were carried out following a method stated in the literature with minor adjustment.[10] An aqueous solution of $Na_2SO_3$ (1 M) was used as the electrolyte. The prepared glass electrode, Ag/AgCl electrode, and Pt electrode were used as the working electrode, reference electrode, and counter electrode, respectively. The experiments were carried out under ambient conditions in the dark and under visible light irradiation (LED, 100 W). For each electrode, LSV and EIS were performed at 100 mV/s in the potential range of −0.7 to 1.5 V and at 0.55 V with a frequency ranging from 1 to $10^6$ Hz, respectively.

## 3. RESULTS AND DISCUSSION

**3.1. X-ray Diffraction.** The crystal structures of the synthesized $Eu(OH)_3$ and $Co-Eu(OH)_3$ NRs were identified by using XRD analysis (Figure 1). All reflections were distinctly

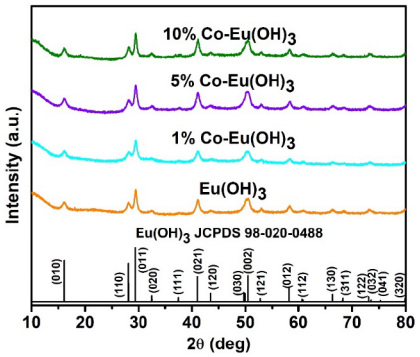


**Figure 1.** XRD patterns of $Eu(OH)_3$ and 1%, 5%, and 10% $Co-Eu(OH)_3$ NRs.

indexed to a pure hexagonal phase (space group = $P6_3/m$) of $Eu(OH)_3$ (JCPDS no. 98−020−0488). Peaks at approximately $2\theta$ = 16.10°, 28.08°, 29.58°, 32.58°, and 41.04° correspond to the (010), (110), (011), (020), and (021) planes, respectively, which is in agreement with the literature.,[18,20,37] There are no other peaks found in $Eu(OH)_3$, 1%, 5%, and 10% $Co-Eu(OH)_3$ NRs suggesting that $Co^{2+}$ ions were successfully incorporated into the lattice and the synthesized $Eu(OH)_3$ NRs were in the pure hexagonal form.

In order to study the influence of Co doping on the structural properties of $Eu(OH)_3$, their average crystallite size was estimated using the Debye−Scherrer equation (eq 2):

$$D = k\lambda/\beta\cos\theta \quad (2)$$

where $\lambda$ denotes the X-ray wavelength, $\theta$ indicates Bragg's angle, and $\beta$ is the fwhm of the peaks. The average crystallite size of $Eu(OH)_3$ was 35.84 nm but when 1% Co was doped into $Eu(OH)_3$ lattice, the average crystallite size was reduced greatly to 21.05 nm (Table 1). The reduction in crystallite size of Co−

**Table 1. Average Crystallite Size (nm), Lattice Parameters (Å), and Cell Volume (Å$^3$) of $Eu(OH)_3$ and $Co-Eu(OH)_3$ NRs**

| samples | average crystallite size (nm) | lattice parameter (Å) | | cell volume (Å$^3$) | average lattice strain ($\varepsilon$) |
|---|---|---|---|---|---|
| | | *a* | *c* | | |
| $Eu(OH)_3$ | 35.84 | 6.36 | 4.19 | 169.48 | 0.0018 |
| 1% $Co-Eu(OH)_3$ | 21.05 | 6.35 | 4.20 | 169.35 | 0.0019 |
| 5% $Co-Eu(OH)_3$ | 23.22 | 6.34 | 4.21 | 169.22 | 0.0021 |
| 10% $Co-Eu(OH)_3$ | 28.32 | 6.34 | 4.21 | 169.22 | 0.0021 |

$Eu(OH)_3$ in comparison to pure $Eu(OH)_3$ might be due to the substitution of $Eu^{3+}$ ions (106 pm) by $Co^{2+}$, which has smaller ionic radii (88.5 pm).[38] However, the average crystallite size was increased slightly to 23.22 and 28.32 nm for both 5% and 10% $Co-Eu(OH)_3$, respectively. This might be due to the decrease in $Eu(OH)_3$ stoichiometry as the substitutional replacement of $Eu^{3+}$ with $Ni^{2+}$ ions was increased.[38]

The average lattice strain was also calculated using the following equation (eq 3):[39,40]

$$\varepsilon = \frac{\beta_{\text{hkl}}}{4\tan\theta} \quad (3)$$

where $\theta$ denotes the diffraction angle and $\beta$ is the fwhm in radians. The average lattice strains for $Eu(OH)_3$ and 1%, 5%, and 10% $Co-Eu(OH)_3$ NRs showed no significant change. Moreover, the cell volumes of $Eu(OH)_3$ and $Co-Eu(OH)_3$ NRs also showed no significant change. Therefore, the incorporation of $Co^{2+}$ (1%, 5%, and 10%) has no major impact on the lattice parameter (*a* and *c*), cell volume, and lattice strain.

**3.2. Fourier Transform Infrared and Raman Spectroscopy.** Different vibrational modes present in $Eu(OH)_3$, 1% $Co-Eu(OH)_3$, 5% $Co-Eu(OH)_3$, and 10% $Co-Eu(OH)_3$ NRs were confirmed by using FT-IR (Figure 2a). The band present at ∼645 cm$^{-1}$ is due to the band vibration of Eu−O−H.[20] As the Co doping level increases, the intensity decreases. This might be due to the successful incorporation of $Co^{2+}$ or substitution of $Eu^{3+}$ with $Co^{2+}$. Symmetric and asymmetric stretching of O−C−O can be observed in all samples at ∼1394 cm$^{-1}$.[18] Absorption bands at 1600 cm$^{-1}$ are assigned to the O−H vibration in absorbed water on the sample surface. Moreover, the stretching and bending of the O−H vibration of $Eu(OH)_3$ and 1%, 5%, and 10% $Co-Eu(OH)_3$ can also be observed at 3550 cm$^{-1}$.

Figure 2b presents the Raman spectra of $Eu(OH)_3$, 1%, and 5% $Co-Eu(OH)_3$ NRs. Three Raman peaks of $Eu(OH)_3$ that were found at 303.22, 377.37, and 485.83 cm$^{-1}$ are assigned to the $A_g$ translatory, $E_{2g}$ translatory, and $E_{1g}$ libration modes, respectively. In general, for hexagonal $Eu(OH)_3$ ($P6_3/m$), the vibrational modes are described as $4A_g + 3B_g + 2E_{1g} + 5E_{2g} + 2A_u + 4B_u + 4E_{1u} + 2E_{2u}$, where $4A_g$, $2E_{1g}$ and $5E_{2g}$ are Raman active.[5] 1% $Co-Eu(OH)_3$ showed lower Raman peak intensity that might be due to the interruption of the lattice constancy and long-range translational crystal symmetry caused by the induced defects in the crystal lattice as stated by Komaraiah et al.[41] In the case of 5% $Co-Eu(OH)_3$, Raman peaks corresponding to the $Eu(OH)_3$ translatory and libration modes broaden, in which three new Raman peaks at 193.30, 480.80, and 519.97 cm$^{-1}$ have


https://doi.org/10.1021/acsomega.3c10416
ACS Omega 2024, 9, 16420−16428

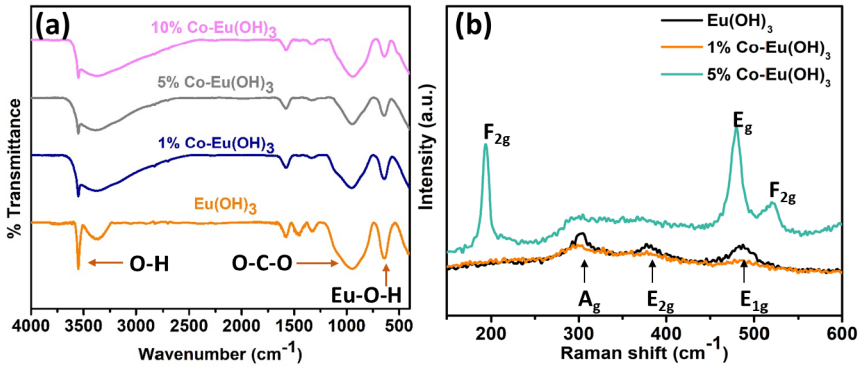


**Figure 2.** *(a)* FT-IR spectra of $Eu(OH)_3$ and 1%, 5%, and 10% Co−$Eu(OH)_3$ NRs and (b) Raman spectra of $Eu(OH)_3$, 1% and 5% Co−$Eu(OH)_3$ NRs.

appeared. These peaks are associated with $3F_{2g}$, $E_g$, and $2F_{2g}$ modes of $Co^{2+}$ ions.[42,43] Therefore, it can be said that $Eu(OH)_3$ and Co−$Eu(OH)_3$ were successfully synthesized.

**3.3. Transmission Electron Microscopy.** Figure 3 exhibits TEM and SAED images of $Eu(OH)_3$, 1%, and 10% Co−$Eu(OH)_3$. It was observed that all samples possess rod-like structure. $Eu(OH)_3$ showed nanorod shape with an average of 27 nm in length and 8 nm in diameter as shown in Figure 3$a_1$. It was observed in many reports that the synthesized $Eu(OH)_3$ showed rod-like shape.[18,20,21,23,44,45] It is stated that the formation of $Eu(OH)_3$ nanorods is due to the rapid formation of small nuclei composed of 1D hexagonal crystal in its anistropic growth nature in supersaturated $Eu^{3+}$ and $OH^-$ solution.[46] Moreover, the hexagonal crystal nuclei will continue to grow under the influence of initial pH, reaction time, and temperature. Figure 3$b_1$ shows the TEM image of 1% Co−$Eu(OH)_3$ NRs with an average length of 33 nm and a diameter of 9 nm. It was observed that the particle size increased when 1% Co was incorporated into $Eu(OH)_3$. The particle size was further increased when 10% Co was incorporated (Figure 3$c_1$). 10% Co−$Eu(OH)_3$ NRs showed an average length of 50 nm and a diameter of 12 nm. This suggests that Co doping has influenced the particle size of $Eu(OH)_3$ as reported in a study by Chanda et al.[47] The difference in the crystal growth velocities in different directions might be the cause for the particle size differences.[47]

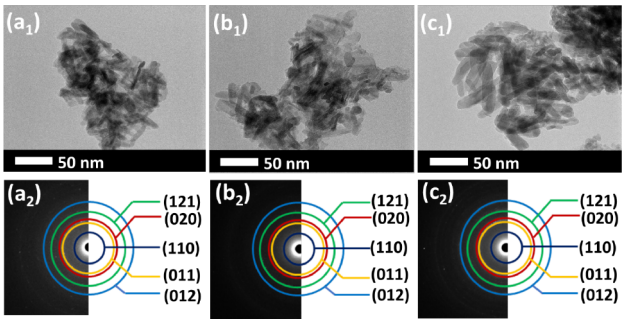


**Figure 3.** TEM images and SAED patterns of $(a_1)$ −$(a_2)$ $Eu(OH)_3$, $(b_1)$−$(b_2)$ 1% Co−$Eu(OH)_3$, and $(c_1)$−$(c_2)$ 10% Co−$Eu(OH)_3$.

Moreover, the nanocrystallinity and diffraction pattern of $Eu(OH)_3$, 1% Co−$Eu(OH)_3$, and 10% Co−$Eu(OH)_3$ NRs are examined by SAED analysis as shown in Figure 3$a_2$,$b_2$, $c_2$. It was observed that $Eu(OH)_3$, 1%, and 10% Co−$Eu(OH)_3$ NRs exhibit five broad rings, which are attributed to the (110), (011), (020), (121), and (012) reflections of the hexagonal $Eu(OH)_3$ ($P6_3/m$) structure. This is in agreement with the XRD results as discussed in an earlier section.

**3.4. UV−vis Diffuse Reflectance Spectroscopy and Photoluminescence Spectroscopy.** The band gap energies of $Eu(OH)_3$ and Co−$Eu(OH)_3$ NRs were estimated using UV−vis DRS analysis. The Tauc plot depicted in Figure 4a was derived from the Kubelka−Munk function (eq 4) as stated below:

$$F(R) = \left(\frac{(1-R)^2}{2R} \times h\nu\right)^{1/2} \quad (4)$$

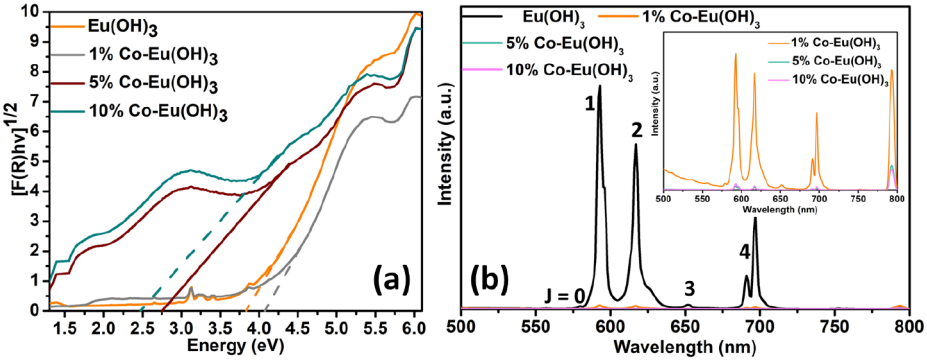


**Figure 4.** (a) Tauc plot obtained from Kubelka−Munk function for the band gap energy estimation and (b) PL spectra of $Eu(OH)_3$ and 1%, 5%, and 10% Co−$Eu(OH)_3$ NRs (inset: the zoomed PL spectra of Co−$Eu(OH)_3$).



https://doi.org/10.1021/acsomega.3c10416
ACS Omega 2024, 9, 16420−16428

where $R$ represents the measured absolute reflectance of the samples. The estimation of the band gap energy can be obtained from the plots of $[F(R)h\nu]^{1/2}$ versus $h\nu$.

The band gap energy of $Eu(OH)_3$ was found to be 3.80 eV, which is in good agreement with the literature.[21] However, when 1% Co was doped into the $Eu(OH)_3$ lattice, the band gap energy was increased to 4.06 eV. Interestingly, further increasing the doping percentage showed a reduction in the band gap energy, in which 5% and 10% Co−$Eu(OH)_3$ showed band gap energies of 2.74 and 2.49 eV, respectively. The band gap energy of higher Co percentage was observed to decrease with the increase in the crystallite size. This might be due to strong quantum confinement in nano-sized crystals.[48] The band gap energies of all samples are tabulated in Table 2.

**Table 2. Band Gap Energy of $Eu(OH)_3$ and Co−$Eu(OH)_3$ NRs**

| sample | band gap energy (eV) |
|---|---|
| $Eu(OH)_3$ | 3.80 |
| 1% Co−$Eu(OH)_3$ | 4.06 |
| 5% Co−$Eu(OH)_3$ | 2.74 |
| 10% Co−$Eu(OH)_3$ | 2.49 |

Photoluminescence analysis of $Eu(OH)_3$ and Co−$Eu(OH)_3$ NRs was carried out to understand the optical behavior of the samples. Figure 4b exhibits the PL emission spectra of $Eu(OH)_3$, 1% Co−$Eu(OH)_3$, 5% Co−$Eu(OH)_3$, and 10% Co−$Eu(OH)_3$ NRs at an excitation wavelength of 370 nm. The resultant emission peaks were found to be in the range 500−800 nm, which are associated with the $^5D_0 \rightarrow {}^7F_j$ ($j$ = 0−4) transitions. Distinct peaks at ∼578, 592, 617, and 651 nm correspond to the $^5D_0 \rightarrow {}^7F_0$, $^5D_0 \rightarrow {}^7F_1$, $^5D_0 \rightarrow {}^7F_2$, and $^5D_0 \rightarrow {}^7F_3$ transitions, respectively. While peaks at 691 and 697 nm corresponds to $^5D_0 \rightarrow {}^7F_4$ transitions.[45] The order of the PL intensity is as follows: $Eu(OH)_3$ > 1% Co−$Eu(OH)_3$ > 5% Co−$Eu(OH)_3$ > 10% Co−$Eu(OH)_3$. The PL intensity dropped significantly when Co was incorporated into the $Eu(OH)_3$ as observed for 1, 5, and 10% Co−$Eu(OH)_3$. In general, PL signal is the result of recombination of photogenerated electron−hole pair. Therefore, high PL intensity indicates more recombination of charge carries, whereas in the case of Co−$Eu(OH)_3$, lower PL intensity suggests the maximum separation of charge carriers.[49]

**3.5. X-Ray Photoelectron Spectroscopy.** XPS of $Eu(OH)_3$, 1%, 5%, and 10% Co−$Eu(OH)_3$ NRs was performed and is presented in Figure 5. The survey scan spectrum shown in Figure 5a confirmed the presence of Co 2$p$, O 1$s$, and Eu 4$d$. The Eu 4$d$ core level peak is shown in Figure 5b. Two major peaks

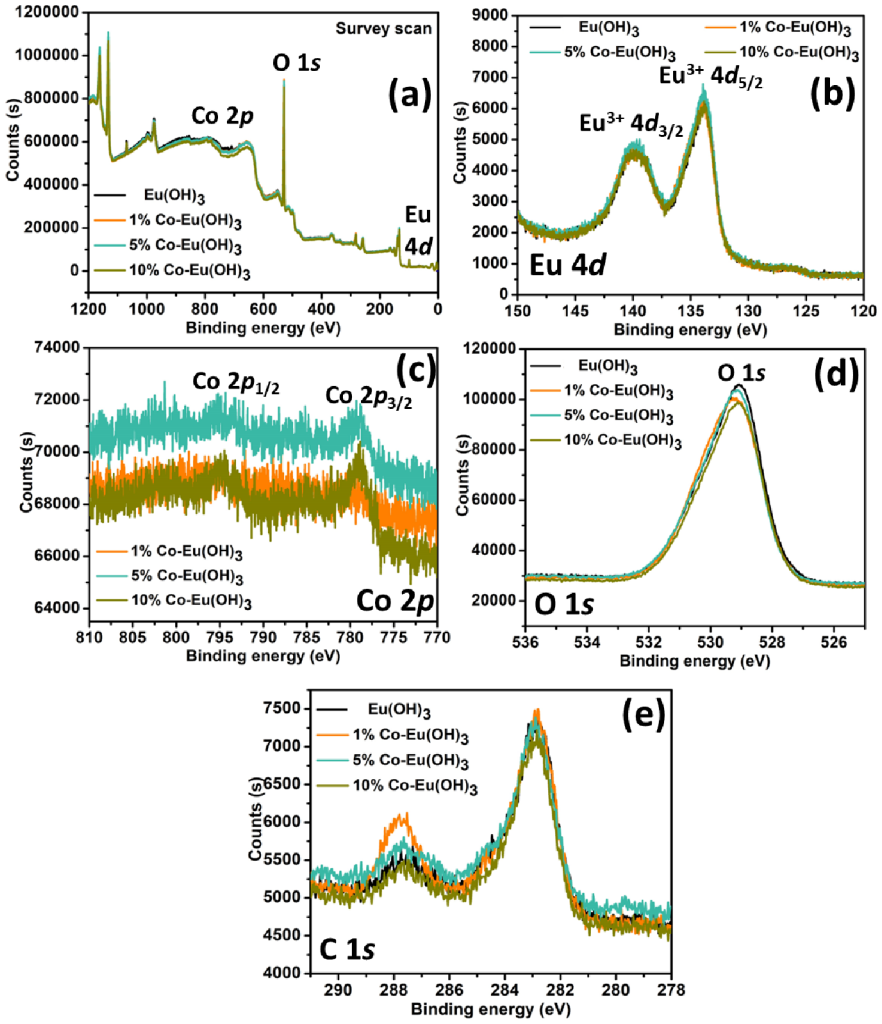


**Figure 5.** XPS spectra: (a) survey scan, (b) Eu 4$d$, (c) Co 2$p$, (d) O 1$s$, and (e) C 1$s$ of $Eu(OH)_3$ and 1%, 5%, and 10% Co−$Eu(OH)_3$ NRs.



https://doi.org/10.1021/acsomega.3c10416
ACS Omega 2024, 9, 16420−16428

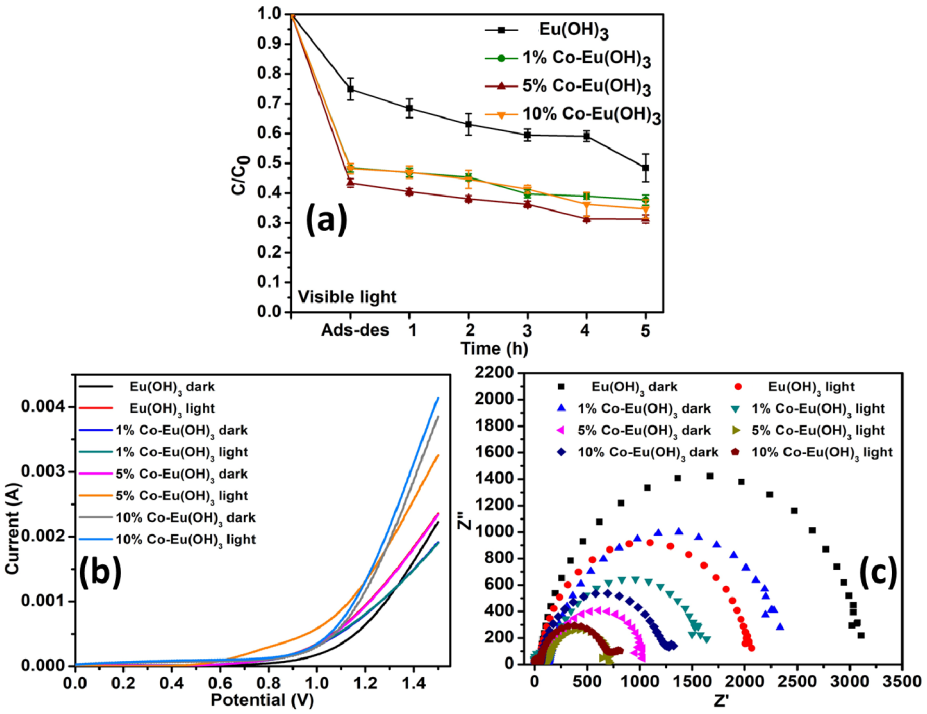


**Figure 6.** (a) The average $C/C_0$ for the photocatalytic degradation of BG under visible light irradiation using $Eu(OH)_3$ and $Co–Eu(OH)_3$ NRs, (b) LSV, and (c) Nyquist plots of $Eu(OH)_3$, 1%, 5%, and 10% $Co–Eu(OH)_3$ photoelectrode in the dark and under visible light irradiation.

**Table 3. Average Percentage Photocatalytic Degradation Activities of $Eu(OH)_3$ and 1%, 5%, and 10% $Co–Eu(OH)_3$ NRs for BG Degradation Under Visible Light Irradiation**

| | % photocatalytic degradation of BG | | | | | |
|---|---|---|---|---|---|---|
| | Ads-des | 1 h | 2 h | 3 h | 4 h | 5 h |
| **$Eu(OH)_3$** | 25.11 ± 3.66 | 31.54 ± 3.17 | 36.94 ± 3.59 | 40.50 ± 1.99 | 40.91 ± 1.77 | 51.50 ± 4.64 |
| **1% $Co–Eu(OH)_3$** | 51.51 ± 1.38 | 53.05 ± 1.45 | 54.68 ± 1.17 | 60.25 ± 1.32 | 61.01 ± 1.01 | 62.35 ± 1.76 |
| **5% $Co–Eu(OH)_3$** | 56.56 ± 1.42 | 59.54 ± 1.08 | 61.93 ± 1.10 | 63.76 ± 1.05 | 68.63 ± 0.96 | 68.69 ± 1.42 |
| **10% $Co–Eu(OH)_3$** | 51.77 ± 1.72 | 52.96 ± 2.08 | 55.36 ± 3.03 | 58.68 ± 1.29 | 63.76 ± 4.05 | 65.32 ± 3.09 |

were observed at approximately 141.9 and 136.2 eV, which correspond to $Eu^{3+}$ $4d_{3/2}$ and $Eu^{3+}$ $4d_{5/2}$, respectively. No significant shift was observed for all samples. Figure 5c shows the XPS spectrum of Co 2*p* of 1%, 5%, and 10% $Co–Eu(OH)_3$ NRs. It can be seen that, 1% $Co–Eu(OH)_3$ shows lower Co 2*p* signal than 5% and 10% $Co–Eu(OH)_3$ NRs. Nevertheless, two peaks were observed at approximately 779.20 and 795.17 eV that are attributed to the Co $2p_{1/2}$ and Co $2p_{3/2}$, respectively.[9]

The XPS spectra of O 1*s* for all samples can be seen in Figure 5d, in which all samples exhibit one major peak only. The peak at approximately 528 eV indicates the nucleophilic oxygen species, which in this case is the $OH^-$ anion.[50] No significant change in the peak position and intensity was observed for all of the samples. The typical C 1*s* was observed in the spectra at ∼283 eV (Figure 5e), which might be derived from the $Eu(CH_3COO)_3 \cdot H_2O$ precursor. The atomic concentrations of C 1*s*, O 1*s*, Eu 3*d*, and Co 2*p* can be found in Table S1.

## 4. APPLICATIONS

**4.1. Photocatalytic Degradation of BG.** The investigation of the photocatalytic degradation of BG was carried out using $Eu(OH)_3$ and 1%, 5%, and 10% $Co–Eu(OH)_3$ NRs under visible light irradiation for 5 h. The absorbance of the reaction solution was measured every hour. The reaction at 0 h shows the adsorption–desorption. Figures S1 and 6a show the average percentage and $C/C_0$ of the photocatalytic degradation of BG using $Eu(OH)_3$ and 1%, 5%, and 10% $Co–Eu(OH)_3$ NRs, respectively.

Based on the results, at adsorption–desorption, 5% $Co–Eu(OH)_3$ showed more adsorption than the other samples, which is about 56%. While $Eu(OH)_3$ showed the lowest average percentage of adsorption–desorption. When irradiated with visible light, 5% $Co–Eu(OH)_3$ showed the highest photocatalytic degradation response with a total of 68% after 5 h reaction as shown in Figure 6a. This is followed by 10% $Co–Eu(OH)_3$, which showed about 65% BG photocatalytic degradation. The effectiveness of the photocatalysts in the photocatalytic degradation of BG was found to be as follows: 5% $Co–Eu(OH)_3$ > 10% $Co–Eu(OH)_3$ > 1% $Co–Eu(OH)_3$ > $Eu(OH)_3$. With respect to their band gap energy, 10% $Co–Eu(OH)_3$ showed the lowest band gap energy (2.49 eV) while 5% $Co–Eu(OH)_3$ showed the second lowest band gap energy (2.74 eV). However, 10% $Co–Eu(OH)_3$ showed the biggest particle size among the samples. Moreover, the PL intensity of 5% $Co–Eu(OH)_3$ (Figure 4b inset) exhibits the lowest intensity indicating the maximum separation of charge carriers, which is very useful for the efficient photocatalytic performance.[51] Hence, 5% $Co–Eu(OH)_3$ NRs showed the highest photocatalytic response. On the other hand, 1% $Co–Eu(OH)_3$ has the highest band gap energy. However, although $Eu(OH)_3$ has a


https://doi.org/10.1021/acsomega.3c10416
ACS Omega 2024, 9, 16420−16428

lower band gap energy than 1% Co−$Eu(OH)_3$, the adsorption affinity of 1% Co−$Eu(OH)_3$ was higher than $Eu(OH)_3$, which facilitated the overall performance of 1% Co−$Eu(OH)_3$ in the photocatalysis. Moreover, particle size and morphology also play some role in enhancing the photocatalytic dye degradation.[52] Therefore, the photocatalytic responses of $Eu(OH)_3$ and Co−$Eu(OH)_3$ NRs were also influenced as can be seen in Figures 6a, S1 and Table 3.

Generally, for a semiconductor, electron ($e^-$) and hole ($h^+$) pairs are generated upon light irradiation.[53] The efficiency of the photocatalytic activity depends on the competition between the recombination and transfer of photogenerated $e^-$ and $h^+$. Reduction in the recombination rate of $e^-/h^+$ pairs is favorable for the enhancement of the photocatalytic efficiency. The general mechanism of photocatalytic degradation of BG has been proposed as follows (**R1 − R5**):

$$\text{Semiconductor} + h\nu \rightarrow e^- + h\nu^+ \quad \text{(R1)}$$

$$O_2 + e^- \rightarrow O_2^{\bullet -} \quad \text{(R2)}$$

$$BG + O_2^{\bullet -} \rightarrow BG_{ox}(\text{intermediates}) \rightarrow CO_2 + H_2O \quad \text{(R3)}$$

$$h^+ + H_2O \rightarrow {}^{\bullet}OH + H^+ \quad \text{(R4)}$$

$$BG + {}^{\bullet}OH \rightarrow BG_{ox}(\text{intermediates}) \rightarrow CO_2 + H_2O \quad \text{(R5)}$$

Under visible light irradiation, $e^-$s are promoted from the valence band (VB) to the conduction band (CB) of $Eu(OH)_3$ leaving $h^+$ in VB. $Eu(OH)_3$ traps electrons, which delays $e^-/h^+$ recombination and increases $O_2^{\bullet -}$ for the degradation of the BG dye. Simultaneously, $^{\bullet}OH$ radicals are formed via the interaction of $h^+$ and surface bound $H_2O$. The $^{\bullet}OH$ radicals are known as a powerful oxidizing agent, which can degrade most of the pollutants.

**4.2. Photoelectrochemical Studies of Co−$Eu(OH)_3$.** The photoelectrochemical studies of $Eu(OH)_3$ and 1%, 5%, and 10% Co−$Eu(OH)_3$ were investigated by using LSV and EIS. LSV analysis was carried out under two conditions: dark and visible light at 100 mV/s in the range of 0−1.5 V as shown in Figure 6b. Each material respectively showed a higher response when irradiated with visible light in comparison to their response in the dark. This suggests that the materials were light responsive. The enhancement in the photocurrent response in Co−$Eu(OH)_3$ especially in the case of 10% Co−$Eu(OH)_3$ NRs was due to the light absorption ability. The formation of a midgap state might be involved in lowering the band gap energy.[54] Moreover, a high photocurrent suggests that the material has a strong ability for the formation and transfer of the photoexcited charge carriers under visible light irradiation.[55]

Figure 6c shows the EIS analysis that was performed at 0.55 V with a frequency ranging from 1 to $10^6$ Hz in the dark and under visible light irradiation. The EIS Nyquist plots show the charge transfer resistance and separation efficiency between the photogenerated electrons and holes.[56] In general, a small arc radius and low resistance indicate higher charge transfer efficiency.[54] $Eu(OH)_3$ showed the biggest arc radius, which indicates lower charge transfer efficiency. When doped with $Co^{2+}$, the arc radius became smaller in the case of Co−$Eu(OH)_3$ NRs, suggesting a higher charge transfer efficiency (Figure 6c). In each case, a significant decrease in the resistance under visible light irradiation suggests that the transfer efficiency of the photogenerated electrons and holes was enhanced.

## 5. CONCLUSIONS

$Eu(OH)_3$ and Co−$Eu(OH)_3$ NRs were prepared using a microwave-assisted synthesis method. The structural, optical, and morphological studies of the $Eu(OH)_3$ and Co−$Eu(OH)_3$ NRs were investigated. Hexagonal phases of $Eu(OH)_3$ were obtained for all the synthesized materials. FT-IR and Raman studies were carried out and the formation of $Eu(OH)_3$ and Co−$Eu(OH)_3$ NRs was confirmed. $Eu(OH)_3$ and Co−$Eu(OH)_3$ NRs were observed with an average length and diameter between 27−50 and 8−12 nm, respectively. Moreover, band gap energies of $Eu(OH)_3$ and Co−$Eu(OH)_3$ NRs were reduced from 3.80 to 2.49 eV and the PL intensities were also quenched strongly with more Co doping. The photocatalytic degradation of BG, and photoelectrochemical studies of the synthesized materials were investigated. 5% Co−$Eu(OH)_3$ NRs showed the highest photocatalytic response under visible light while the photoelectrochemical studies showed that 10% Co−$Eu(OH)_3$ NRs have enhanced response under visible light irradiation. Therefore, Co−$Eu(OH)_3$ NRs have the potential to be used as a visible-light active material for photocatalysis.

## ■ ASSOCIATED CONTENT

### Data Availability Statement

The data are available throughout the manuscript and supporting file.

### Supporting Information

The Supporting Information is available free of charge at https://pubs.acs.org/doi/10.1021/acsomega.3c10416.

The average percentage of photocatalytic degradation of BG using $Eu(OH)_3$ and Co−$Eu(OH)_3$ NRs (Figure S1). The atomic concentration of C 1*s*, O 1*s*, Eu 4*d*, and Co 2*p* of $Eu(OH)_3$, 1%, 5%, and 10% Co−$Eu(OH)_3$ NRs (Table S1) (PDF)

## ■ AUTHOR INFORMATION


### Corresponding Author

**Mohammad Mansoob Khan** − *Chemical Sciences, Faculty of Science, Universiti Brunei Darussalam, Gadong BE 1410, Brunei Darussalam*; orcid.org/0000-0002-8633-7493; Email: mmansoobkhan@yahoo.com, mansoob.khan@ubd.edu.bn

### Authors

**Shaidatul Najihah Matussin** − *Chemical Sciences, Faculty of Science, Universiti Brunei Darussalam, Gadong BE 1410, Brunei Darussalam*

**Fazlurrahman Khan** − *Institute of Fisheries Sciences, Pukyong National University, Busan 48513, Republic of Korea; Marine Integrated Biomedical Technology Center, The National Key Research Institutes in Universities, Pukyong National University, Busan 48513, Republic of Korea; Research Center for Marine Integrated Bionics Technology, Pukyong National University, Busan 48513, Republic of Korea*

**Mohammad Hilni Harunsani** − *Chemical Sciences, Faculty of Science, Universiti Brunei Darussalam, Gadong BE 1410, Brunei Darussalam*

**Young-Mog Kim** − *Marine Integrated Biomedical Technology Center, The National Key Research Institutes in Universities, Pukyong National University, Busan 48513, Republic of Korea; Research Center for Marine Integrated Bionics Technology, Pukyong National University, Busan 48513, Republic of Korea; Department of Food Science and*




https://doi.org/10.1021/acsomega.3c10416
ACS Omega 2024, 9, 16420−16428

*Technology, Pukyong National University, Busan 48513, Republic of Korea;* orcid.org/0000-0002-2465-8013

Complete contact information is available at: https://pubs.acs.org/10.1021/acsomega.3c10416

### Author Contributions

S.N.M.: Methodology; Investigation, Data curation; Writing—original draft. F.K.: Methodology, Investigation, Data curation. M.H.H.: Supervision, Writing—review and editing. Y.-M.K.: Resources, Formal analysis. M.M.K.: Supervision, Conceptualization, Funding acquisition, Writing—review and editing.

### Notes

The authors declare no competing financial interest.

## ■ ACKNOWLEDGMENTS

The authors would like to acknowledge the FRC grant (UBD/RSCH/1.4/FICBF(b)/2023/059) received from Universiti Brunei Darussalam, Brunei Darussalam. This research was also supported by Basic Science Research Program through the National Research Foundation of Korea (NRF) grant funded by the Ministry of Education (2021R1A6A1A03039211 and 2022R1A2B5B01001998).

## ■ REFERENCES

(1) Mo, Z.; Deng, Z.; Guo, R.; Fu, Q.; Feng, C.; Liu, P.; Sun, Y. Synthesis and Luminescence Properties for Europium Oxide Nanotubes. *Mater. Sci. Eng. B Solid State Mater. Adv. Technol.* **2012**, *177* (1), 121−126.

(2) Khan, M. M.; Matussin, S. N. Sm $_2$ O $_3$ and Sm $_2$ O $_3$ -Based Nanostructures for Photocatalysis, Sensors, CO Conversion, and Biological Applications. *Catal. Sci. Technol.* **2023**, *13* (8), 2274−2290.

(3) Matussin, S. N.; Harunsani, M. H.; Khan, M. M. $CeO_2$ and $CeO_2$-Based Nanomaterials for Photocatalytic, Antioxidant and Antimicrobial Activities. *J. Rare Earths* **2023**, *41* (2), 167−181.

(4) Abdulwahab, K. O.; Khan, M. M.; Jennings, J. R. Doped Ceria Nanomaterials: Preparation, Properties, and Uses. *ACS Omega* **2023**, *8* (34), 30802−30823.

(5) Mu, Q.; Wang, Y. A Simple Method to Prepare $Ln(OH)_3$ (Ln = La, Sm, Tb, Eu, and Gd) Nanorods Using CTAB Micelle Solution and Their Room Temperature Photoluminescence Properties. *J. Alloys Compd.* **2011**, *509* (5), 2060−2065.

(6) Patil, A. S.; Patil, A. V.; Dighavkar, C. G.; Adole, V. A.; Tupe, U. J. Synthesis Techniques and Applications of Rare Earth Metal Oxides Semiconductors: A Review. *Chem. Phys. Lett.* **2022**, *796*, 139555.

(7) Hou, Z.; Pei, W.; Zhang, X.; Zhang, K.; Liu, Y.; Deng, J.; Jing, L.; Dai, H. Rare Earth Oxides and Their Supported Noble Metals in Application of Environmental Catalysis. *J. Rare Earths* **2020**, *38* (8), 819−839.

(8) Patil, A. S.; Patil, A. V.; Dighavkar, C. G.; Adole, V. A.; Tupe, U. J. Synthesis Techniques and Applications of Rare Earth Metal Oxides Semiconductors: A Review. *Chem. Phys. Lett.* **2022**, *796*, 139555.

(9) Matussin, S. N.; Khan, F.; Harunsani, M. H.; Kim, Y.-M.; Khan, M. M. Visible-Light-Induced Photocatalytic and Photoantibacterial Activities of Co-Doped CeO $_2$. *ACS Omega* **2023**, *8* (13), 11868−11879.

(10) Matussin, S. N.; Khan, F.; Harunsani, M. H.; Kim, Y.-M.; Khan, M. M. Effect of Pd-Doping Concentrations on the Photocatalytic, Photoelectrochemical, and Photoantibacterial Properties of $CeO_2$. *Catalysts* **2023**, *13* (1), 96.

(11) Kaszewski, J.; Witkowski, B. S.; Wachnicki, Ł.; Przybylińska, H.; Kozankiewicz, B.; Mijowska, E.; Godlewski, M. Luminescence Enhancement in Nanocrystalline $Eu_2O_3$ Nanorods − Microwave Hydrothermal Crystallization and Thermal Degradation of Cubic Phase. *Opt. Mater.* **2016**, *59*, 76−82.

(12) Bhuvanendran, N.; Ravichandran, S.; Kandasamy, S.; Zhang, W.; Xu, Q.; Khotseng, L.; Maiyalagan, T.; Su, H. Spindle-Shaped $CeO_2$/Biochar Carbon with Oxygen-Vacancy as an Effective and Highly Durable Electrocatalyst for Oxygen Reduction Reaction. *Int. J. Hydrogen Energy* **2021**, *46* (2), 2128−2142.

(13) Vidya, Y. S.; Anantharaju, K. S.; Nagabhushana, H.; Sharma, S. C. Euphorbia Tirucalli Mediated Green Synthesis of Rose like Morphology of $Gd_2O_3$:$Eu^{3+}$ Red Phosphor: Structural, Photoluminescence and Photocatalytic Studies. *J. Alloys Compd.* **2015**, *619*, 760−770.

(14) Vijayaprasath, G.; Habibulla, I.; Dharuman, V.; Balasubramanian, S.; Ganesan, R. Fabrication of $Gd_2O_3$Nanosheet-Modified Glassy Carbon Electrode for Nonenzymatic Highly Selective Electrochemical Detection of Vitamin B2. *ACS Omega* **2020**, *5* (29), 17892−17899.

(15) Matussin, S. N.; Rahman, A.; Khan, M. M. Role of Anions in the Synthesis and Crystal Growth of Selected Semiconductors. *Front. Chem.* **2022**, *10*, 881518.

(16) Hadamek, T.; Rangan, S.; Viereck, J.; Shin, D.; Posadas, A. B.; Bartynski, R. A.; Demkov, A. A. Stoichiometry, Band Alignment, and Electronic Structure of $Eu_2O_3$ Thin Films Studied by Direct and Inverse Photoemission: A Reevaluation of the Electronic Band Structure. *J. Appl. Phys.* **2020**, *127* (7), 074101.

(17) Kumar, S.; Prakash, R.; Choudhary, R. J.; Phase, D. M. Structural, Morphological and Electronic Properties of Pulsed Laser Grown $Eu_2O_3$ Thin Films. *AIP Conf. Proc.* **2018**, *1953*, 100012.

(18) Kang, J.-G.; Jung, Y.; Min, B.-K.; Sohn, Y. Full Characterization of $Eu(OH)_3$ and $Eu2_{O3}$ Nanorods. *Appl. Surf. Sci.* **2014**, *314*, 158−165.

(19) Feng, J.; Zhang, H. Hybrid Materials Based on Lanthanide Organic Complexes: A Review. *Chem. Soc. Rev.* **2013**, *42* (1), 387−410.

(20) Ji, X.; Hu, P.; Li, X.; Zhang, L.; Sun, J. Hydrothermal Control, Characterization, Growth Mechanism, and Photoluminescence Properties of Highly Crystalline 1D $Eu(OH)_3$nanostructures. *RSC Adv.* **2020**, *10* (55), 33499−33508.

(21) Liu, S.; Cai, Y.; Cai, X.; Li, H.; Zhang, F.; Mu, Q.; Liu, Y.; Wang, Y. Catalytic Photodegradation of Congo Red in Aqueous Solution by $Ln(OH)_3$ (Ln = Nd, Sm, Eu, Gd, Tb, and Dy) Nanorods. *Appl. Catal., A* **2013**, *453*, 45−53.

(22) Pastor, A.; Chen, C.; de Miguel, G.; Martín, F.; Cruz-Yusta, M.; O'Hare, D.; Pavlovic, I.; Sánchez, L. Facile Synthesis of Visible-Responsive Photocatalytic Eu-Doped Layered Double Hydroxide for Selective Removal of NOx Pollutant. *Chem. Eng. J.* **2023**, *471*, 144464.

(23) Wei, P.-F.; Zhang, L.; Nethi, S. K.; Barui, A. K.; Lin, J.; Zhou, W.; Shen, Y.; Man, N.; Zhang, Y.-J.; Xu, J.; Patra, C. R.; Wen, L.-P. Accelerating the Clearance of Mutant Huntingtin Protein Aggregates through Autophagy Induction by Europium Hydroxide Nanorods. *Biomaterials* **2014**, *35* (3), 899−907.

(24) Zhang, D.; Yan, T.; Shi, L.; Li, H.; Chiang, J. F. Template-Free Synthesis, Characterization, Growth Mechanism and Photoluminescence Property of $Eu(OH)_3$ and $Eu_2O_3$ Nanospindles. *J. Alloys Compd.* **2010**, *506* (1), 446−455.

(25) Shih, K. Y.; Yu, S. C. Microwave-Assisted Rapid Synthesis of Eu(Oh)3/Rgo Nanocomposites and Enhancement of Their Antibacterial Activity against *Escherichia Coli*. *Materials* **2022**, *15* (1), 43.

(26) Ansari, A. A.; Hasan, T. N.; Syed, N. A.; Labis, J. P.; Parchur, A. K.; Shafi, G.; Alshatwi, A. A. In-Vitro Cyto-Toxicity, Geno-Toxicity, and Bio-Imaging Evaluation of One-Pot Synthesized Luminescent Functionalized Mesoporous $SiO_2$@$Eu(OH)_3$ Core-Shell Microspheres. *Nanomedicine* **2013**, *9* (8), 1328−1335.

(27) Liu, W.; Zhang, J.; Yin, X.; He, X.; Wang, X.; Wei, Y. Luminescent Layered Europium Hydroxide as Sensor for Multi-Response to $Cr_2O_7^{2-}$ or $MnO_4^-$ Based on Static Quenching and Inner Filter Effect. *Mater. Chem. Phys.* **2021**, *266*, 124540.

(28) Cacciotti, I. Cationic and Anionic Substitutions in Hydroxyapatite. In *Handbook of Bioceramics and Biocomposites*; Springer International Publishing: Cham, 2016; pp 145−211. DOI: .

(29) Chiu, Y.-H.; Chang, T.-F.; Chen, C.-Y.; Sone, M.; Hsu, Y.-J. Mechanistic Insights into Photodegradation of Organic Dyes Using Heterostructure Photocatalysts. *Catalysts* **2019**, *9* (5), 430.

(30) Thambiraj, S.; Sharmila, G.; Ravi Shankaran, D. Green Adsorbents from Solid Wastes for Water Purification Application. *Mater. Today Proc.* **2018**, *5* (8), 16675−16683.

(31) Rafiq, A.; Ikram, M.; Ali, S.; Niaz, F.; Khan, M.; Khan, Q.; Maqbool, M. Photocatalytic Degradation of Dyes Using Semiconductor Photocatalysts to Clean Industrial Water Pollution. *J. Ind. Eng. Chem.* **2021**, *97*, 111−128.
(32) Beitollahi, H.; van Le, Q.; Farha, O. K.; Shokouhimehr, M.; Tajik, S.; Nejad, F. G.; Kirlikovali, K. O.; Jang, H. W.; Varma, R. S. Recent Electrochemical Applications of Metal-Organic Framework- Based Materials. *Cryst. Growth Des.* **2020**, *20*, 7034−7064.
(33) Basu, K.; Benetti, D.; Zhao, H.; Jin, L.; Vetrone, F.; Vomiero, A.; Rosei, F. Enhanced Photovoltaic Properties in Dye Sensitized Solar Cells by Surface Treatment of $SnO_2$ Photoanodes. *Sci. Rep.* **2016**, *6*, 1−10.
(34) Li, L.; Zhu, B.; Zhang, J.; Yan, C.; Wu, Y. Electrical Properties of Nanocube $CeO_2$ in Advanced Solid Oxide Fuel Cells. *Int. J. Hydrogen Energy* **2018**, *43* (28), 12909−12916.
(35) Liang, S.; Wang, H.; Li, Y.; Qin, H.; Luo, Z.; Huang, B.; Zhao, X.; Zhao, C.; Chen, L. Rare-Earth Based Nanomaterials and Their Composites as Electrode Materials for High Performance Supercapacitors: A Review. *Sustain Energy Fuels* **2020**, *4* (8), 3825−3847.
(36) Xie, W.; Liu, B.; Xiao, S.; Li, H.; Wang, Y.; Cai, D.; Wang, D.; Wang, L.; Liu, Y.; Li, Q.; Wang, T. High Performance Humidity Sensors Based on $CeO_2$Nanoparticles. *Sens. Actuators, B Chem.* **2015**, *215*, 125−132.
(37) Lee, D.; Seo, J.; Valladares, L. D. L. S.; Avalos Quispe, O.; Barnes, C. H. W. Magnetic and Structural Properties of Yellow Europium Oxide Compound and $Eu(OH)_3$. *J. Solid State Chem.* **2015**, *228*, 141−145.
(38) Abbas, F.; Iqbal, J.; Jan, T.; Naqvi, M. S. H.; Gul, A.; Abbasi, R.; Mahmood, A.; Ahmad, I.; Ismail, M. Differential Cytotoxicity of Ferromagnetic Co Doped $CeO_2$ Nanoparticles against Human Neuroblastoma Cancer Cells. *J. Alloys Compd.* **2015**, *648*, 1060−1066.
(39) Matussin, S. N.; Harunsani, M. H.; Tan, A. L.; Cho, M. H.; Khan, M. M. Effect of $Co^{2+}$ and $Ni^{2+}$ Co-Doping on $SnO_2$ Synthesized via Phytogenic Method for Photoantioxidant Studies and Photoconversion of 4-Nitrophenol. *Mater. Today Commun.* **2020**, *25*, 101677.
(40) Matussin, S. N.; Tan, A. L.; Harunsani, M. H.; Cho, M. H.; Khan, M. M. Green and Phytogenic Fabrication of Co-Doped $SnO_2$ Using Aqueous Leaf Extract of Tradescantia Spathacea for Photoantioxidant and Photocatalytic Studies. *Bionanoscience* **2021**, *11* (1), 120−135.
(41) Komaraiah, D.; Radha, E.; James, J.; Kalarikkal, N.; Sivakumar, J.; Ramana Reddy, M. V.; Sayanna, R. Effect of Particle Size and Dopant Concentration on the Raman and the Photoluminescence Spectra of $TiO^2$:Eu 3+ Nanophosphor Thin Films. *J. Lumin.* **2019**, *211*, 320−333.
(42) UmaSudharshini, A.; Bououdina, M.; Venkateshwarlu, M.; Dhamodharan, P.; Manoharan, C. Solvothermal Synthesis of Cu-Doped $Co_3O_4$ Nanosheets at Low Reaction Temperature for Potential Supercapacitor Applications. *Appl. Phys. A* **2021**, *127* (5), 1.
(43) Wang, Y.; Wei, X.; Hu, X.; Zhou, W.; Zhao, Y. Effect of Formic Acid Treatment on the Structure and Catalytic Activity of $Co_3O_4$ for $N_2O$ Decomposition. *Catal. Lett.* **2019**, *149* (4), 1026−1036.
(44) Tian, C.; Wang, L.; Luan, F.; Fu, X.; Zhuang, X.; Chen, L. A Novel Electrochemiluminescent Emitter of Europium Hydroxide Nanorods and Its Application in Bioanalysis. *Chem. Commun.* **2019**, *55* (83), 12479−12482.
(45) Zeng, Q. G.; Ding, Z. J.; Zhang, Z. M.; Sheng, Y. Q. Photoluminescence and Raman Spectroscopy Studies of $Eu(OH)_3$ Rods at High Pressures. *J. Phys. Chem. C* **2010**, *114* (11), 4895−4900.
(46) Parchur, A. K.; Ningthoujam, R. S. Preparation and Structure Refinement of $Eu^{3+}$ Doped $CaMoO_4$ Nanoparticles. *Dalton Trans.* **2011**, *40* (29), 7590.
(47) Chanda, A.; Gupta, S.; Vasundhara, M.; Joshi, S. R.; Mutta, G. R.; Singh, J. Study of Structural, Optical and Magnetic Properties of Cobalt Doped ZnO Nanorods. *RSC Adv.* **2017**, *7* (80), 50527−50536.
(48) Khammar, M.; Ynineb, F.; Guitouni, S.; Bouznit, Y.; Attaf, N. Crystallite Size and Intrinsic Strain Contribution in Band Gap Energy Redshift of Ultrasonic-Sprayed Kesterite CZTS Nanostructured Thin Films. *Appl. Phys. A* **2020**, *126* (6), 398.
(49) Kadam, A. N.; Lee, J.; Nipane, S. V.; Lee, S.-W. Nanocomposites for Visible Light Photocatalysis. In *Nanostructured Materials for Visible Light Photocatalysis*; Elsevier, 2022; pp 295−317. DOI: .
(50) Jones, T. E.; Rocha, T. C. R.; Knop-Gericke, A.; Stampfl, C.; Schlögl, R.; Piccinin, S. Thermodynamic and Spectroscopic Properties of Oxygen on Silver under an Oxygen Atmosphere. *Phys. Chem. Chem. Phys.* **2015**, *17* (14), 9288−9312.
(51) Kadam, A. N.; Lee, J.; Nipane, S. V.; Lee, S.-W. Nanocomposites for Visible Light Photocatalysis. In *Nanostructured Materials for Visible Light Photocatalysis*; Elsevier, 2022; pp 295−317. DOI: .
(52) Li, D.; Song, H.; Meng, X.; Shen, T.; Sun, J.; Han, W.; Wang, X. Effects of Particle Size on the Structure and Photocatalytic Performance by Alkali-Treated $TiO_2$. *Nanomaterials* **2020**, *10* (3), 546.
(53) Khan, M. M. Principles and Mechanisms of Photocatalysis. In *Photocatalytic Systems by Design*; Elsevier, 2021; pp 1−22. DOI: .
(54) Khan, M. M.; Ansari, S. A.; Pradhan, D.; Ansari, M. O.; Han, D. H.; Lee, J.; Cho, M. H. Band Gap Engineered $TiO_2$ Nanoparticles for Visible Light Induced Photoelectrochemical and Photocatalytic Studies. *J. Mater. Chem. A Mater.* **2014**, *2* (3), 637−644.
(55) Lu, X.; Zheng, D.; Zhang, P.; Liang, C.; Liu, P.; Tong, Y. Facile Synthesis of Free-Standing $CeO_2$ Nanorods for Photoelectrochemical Applications. *Chem. Commun.* **2010**, *46* (41), 7721.
(56) Ansari, S. A.; Khan, M. M.; Ansari, M. O.; Kalathil, S.; Lee, J.; Cho, M. H. Band Gap Engineering of $CeO_2$ Nanostructure Using an Electrochemically Active Biofilm for Visible Light Applications. *RSC Adv.* **2014**, *4* (32), 16782−16791.


https://doi.org/10.1021/acsomega.3c10416
*ACS Omega* 2024, 9, 16420−16428